Williams Robin Simon Brooke (Orcid ID: 0000-0002-9826-6020)

Title:

Structural basis of AMPA receptor inhibition by 4-BCCA

Running Title:

Structural basis of AMPA receptor inhibition by 4-BCCA

Maria V. Yelshanskaya[1], Appu K. Singh[1,2], Chamali Narangoda[3], Robin S. B. Williams[4], Maria G. Kurnikova[3] and Alexander I. Sobolevsky[1]

[1]Department of Biochemistry and Molecular Biophysics, Columbia University 650 West 168th Street, New York, NY 10032

[2]Department of Biological Sciences and Bioengineering, Indian Institute of Technology, Kanpur 208016, India

[3]Chemistry Department, Carnegie Mellon University, 4400 Fifth Ave, Pittsburgh, PA 15213

[4]Centre for Biomedical Sciences, School of Biological Sciences, Royal Holloway University of London, Egham TW20 0EX, UK

Correspondence and requests for materials should be addressed to A.I.S.

(Email: as4005@cumc.columbia.edu; Tel: 212-305-4249; Fax: 212-304-5534)

Word count: 6,090

This article has been accepted for publication and undergone full peer review but has not been through the copyediting, typesetting, pagination and proofreading process which may lead to differences between this version and the Version of Record. Please cite this article as doi: 10.1111/bph.15254

ACKNOWLEDGEMENTS

We thank the personnel at the Advanced Photon Source (APS) beamlines 24-ID-C/E. M.G.K. is supported by the NIH (R01 NS083660, R01 GM128195) and NSF (1818213). A.I.S. is supported by the NIH (R01 CA206573, R01 NS083660, R01 NS107253), NSF (1818086) and the Irma T. Hirschl Career Scientist Award. X-ray diffraction data collection was conducted at the Northeastern Collaborative Access Team beamlines, which are funded by the National Institute of General Medical Sciences from the National Institutes of Health (P30 GM124165). The Pilatus 6M detector on 24-ID-C beam line is funded by a NIH-ORIP HEI grant (S10 RR029205). This research used resources of the APS, a U.S. Department of Energy (DOE) Office of Science User Facility operated for the DOE Office of Science by Argonne National Laboratory under Contract No. DE-AC02-06CH11357.

AUTHOR CONTRIBUTIONS

M.V.Y. and A.I.S. designed the project. M.V.Y. expressed and purified protein, carried out mutagenesis and electrophysiological recordings. M.V.Y. and A.K.S. performed crystallographic experiments. C.N. and M.G.K carried out molecular modelling. R.S.B.W. contributed to the study concept and provided 4-BCCA. M.V.Y., A.K.S., C.N., R.S.B.W., M.G.K. and A.I.S. contributed to manuscript writing.

CONFLICT OF INTEREST

RSBW holds two patents (WO2016038379A1 and WO2019002435A1) related to this paper. The remaining authors declare no conflicts of interest.

DECLARATION OF TRANSPARENCY AND SCIENTIFIC RIGOUR

This Declaration acknowledges that this paper adheres to the principles for transparent reporting and scientific rigour as stated in the BJP guidelines and as recommended by funding agencies, publishers and other organizations engaged with supporting research.

ACCESSION NUMBER

The atomic coordinates and structure factors have been deposited to the Protein Data Bank under the accession code 6XSR (see Table 1 for detail).

ABSTRACT

Background and Purpose: AMPA receptors, which shape excitatory postsynaptic currents and are directly involved in overactivation of synaptic function during seizures, represent a well-accepted target for antiepileptic drugs (AEDs). Trans-4-butylcyclohexane carboxylic acid (4-BCCA) has emerged as a new promising AED in multiple *in vitro* and *in vivo* seizure models but the mechanism of its action remained unknown. The purpose of this study is to characterize structure and dynamics of 4-BCCA interaction with AMPA receptors.

Experimental Approach: We studied the molecular mechanism of AMPA receptor inhibition by 4-BCCA using a combination of X-ray crystallography, mutagenesis, electrophysiology and molecular dynamics simulations.

Key Results: We identified 4-BCCA binding sites in the transmembrane domain (TMD) of AMPA receptor, at the lateral portals formed by transmembrane segments M1-M4. At this binding site, 4-BCCA is very dynamic, assumes multiple poses and can enter the ion channel pore.

Conclusion and Implications: 4-BCCA represents a low-affinity inhibitor of AMPA receptors that acts at the TMD sites distinct from noncompetitive inhibitors, such as AED perampanel, and ion channel blockers. Future studies might examine a possibility of synergistic use of these inhibitors in treatment of epilepsy and a wide range of neurological disorders and gliomas.

Keywords: AMPA receptors, iGluRs, inhibition, transmembrane domain, X-ray crystallography, antiepileptic drugs, trans-4-butylcyclohexane carboxylic acid (4-BCCA), decanoic acid, medium chain triglyceride (MCT) diet, perampanel, electrophysiology, patch-clamp, molecular dynamics (MD) simulations.

1. INTRODUCTION

AMPA receptors, a subtype of ionotropic glutamate receptors, represent a well-accepted target for AEDs (Rogawski, 2011). They play a pivotal role in conducting postsynaptic currents and are thus essential for the over activation of synaptic function during seizures. The first approved drug treatment for epilepsy based upon AMPA receptor inhibition was perampanel (Fycompa; PMP), a noncompetitive AMPA receptor antagonist that is used as an adjunctive treatment for partial-onset and primary generalised tonic-clonic seizures (Frampton, 2015). The binding site for PMP on AMPA receptors has been well characterised, providing insight to how it inhibits receptor function (Chang et al., 2016; Narangoda, Sakipov & Kurnikova, 2019; Yelshanskaya, Singh, Sampson, Narangoda, Kurnikova & Sobolevsky, 2016; Yuan, Shi, Srinivasan, Ptak, Oswald & Nowak, 2019). However, PMP has dose-dependent behavioural side-effects, limiting its use in some patients (Rugg-Gunn, 2014).

Further interest in AMPA receptors as a molecular target in epilepsy treatment arose following the identification that these receptors are inhibited by a component of the medium chain triglyceride (MCT) diet that is used in the treatment of patients with drug resistant epilepsy (Neal et al., 2009). Although this diet was considered to function through ketone generation for seizure control (Augustin et al., 2018a; Bough & Rho, 2007), recent studies have shown a direct anti-seizure effect of decanoic acid (or capric acid; Figure 1) provided in this diet through the non-competitive inhibition of AMPA receptors (Chang et al., 2016; Chang et al., 2012; Chang et al., 2015; Wlaz et al., 2015). Interestingly, decanoic acid was suggested to bind to AMPA receptors at a site distinct to that of PMP (Chang et al., 2016). This was confirmed when combinatory treatment using both PMP and decanoic acid was found to directly inhibit AMPA receptors in a synergistic manner, and to synergistically inhibit seizure-like activity in rodent and human brain slice experiments (Augustin et al., 2018b). These data

strongly suggest a direct binding site for decanoic acid and PMP on AMPA receptors, with inhibiting at both sites reducing seizure-like activity.

Due to the restrictions with dietary interventions, a search for drug-based approaches to reproduce the molecular mechanism of the MCT diet was pursued. Novel compound screening employed a range of structures related to both decanoic acid and the widely used AED, valproate, included assessment of their ability to inhibit seizure-associate changes in phosphoinositide turnover (Chang et al., 2012; Chang, Walker & Williams, 2014), and direct inhibition of AMPA receptors (Chang et al., 2016), with effectiveness in multiple *in vitro* and *in vivo* seizure models (Chang et al., 2012; Chang, Terbach, Plant, Chen, Walker & Williams, 2013; Chang et al., 2015; Warren, Walker & Williams, 2018). The most promising of these compounds (trans-4-butylcyclohexane carboxylic acid; 4-BCCA; Figure 1) showed strong activity in multiple *in vitro* and *in vivo* seizure models associated with distinct seizure types (Chang et al., 2012; Chang, Terbach, Plant, Chen, Walker & Williams, 2013; Chang et al., 2015; Warren, Walker & Williams, 2018) (Barker-Haliski, 2019): the mouse psychomotor seizure model reflecting partial or focal epilepsy syndromes (6Hz model: ED_{50} 81 mg/kg); the mouse corneal-kindled model reflecting pharmacoresistant epilepsy with chronic seizures that exhibits behavioral and neuropathological changes of epilepsy (CDK model: ED_{50} 44 mg/kg); the rat maximal electroshock model for generalized tonic clonic seizures (MES model: ED_{50} ~100 mg/kg) and the mouse subcutaneous metrazol seizure threshold test model of a clonic, forebrain seizure (scMES model: ED_{50} ~150 mg/kg). In all of these models, 4-BCCA showed enhanced potency over valproate (Chang et al., 2015). Importantly, this compound lacked the teratogenic-associated effect of histone deacetylase (HDAC) inhibition (Chang et al., 2015), widely shown for valproate (Gottlicher et al., 2001; Gurvich, Tsygankova, Meinkoth & Klein, 2004) that causes a range of detrimental developmental and neurological outcomes (Alsdorf & Wyszynski, 2005). These data provide a strong rationale for the continued analysis and

development of 4-BCCA as a replacement AED for valproate. A clear understanding of the mechanism of AMPA receptor inhibition and synergistic inhibition with PMP will improve our understanding of the important new AED.

2. METHODS

2.1 Constructs and expression

In our experiments, we used rat GluA2i (flip) (NP_058957) subunit (also known as GluRBi or GluR2i) (Hollmann, O'Shea-Greenfield, Rogers & Heinemann, 1989; Keinänen et al., 1990), which has an amino acid sequence 99.7% identical overall and 100% identical in the transmembrane region (where 4-BCCA binding sites are located) to human GluA2i. Rat GluA2i was introduced with its native signal peptide into the pEG BacMam vector for expression in baculovirus-transduced HEK293 GnTI^{-} cells (Goehring et al., 2014). The construct, which we used for crystallization and structure determination, GluA2$_{Del}$, was described previously (Yelshanskaya, Singh, Sampson, Narangoda, Kurnikova & Sobolevsky, 2016) and included additional modifications. For purification and fluorescence detection purposes, coding sequences for a thrombin cleavage site (GLVPRG), an enhanced green fluorescent protein (eGFP) (Cormack, Valdivia & Falkow, 1996) and a Strep-tag (WSHPQFEK) were introduced at the carboxyl terminus. To improve crystallization behaviour of GluA2$_{Del}$, 36 residues were removed from the carboxyl-terminus, 6 residues (L378, T379, L381, P382, S383, and G384; numbering according to the mature polypeptide sequence) were deleted from the ATD-LBD polypeptide linker, three of four predicted *N*-linked glycosylation sites were knocked-out (N235E, N385D and N392Q), the 22 residue-long M1-M2 linker was replaced with the 3-residue DTD linker, the R586Q mutation at the Q/R site (Sommer, Kohler, Sprengel & Seeburg, 1991), which makes GluA2 receptors calcium permeable (Burnashev, Monyer, Seeburg & Sakmann, 1992; Hume, Dingledine & Heinemann, 1991), was introduced

to stabilize the tetrameric state of the receptor and the C589A mutation was introduced to reduce non-specific disulfide bond formation (Sobolevsky, Rosconi & Gouaux, 2009).

2.2 Purification

HEK293 GnTI$^-$ cells were harvested 60-96 hours after addition of BacMam P2 virus and collected by a low-speed centrifugation (6000 rpm, 10 min). Cells were disrupted using a Misonix Sonicator (18 × 15 s, power level 7) in a buffer containing 150 mM NaCl, 20 mM Tris-HCl (pH 8.0), 0.8 μM aprotinin, 2 μg/ml leupeptin, 2 μM pepstatin A and 1 mM phenylmethylsulfonyl fluoride (25 ml buffer/1L HEK293 culture). The homogenate was clarified using a Sorval centrifuge (8000 rpm, 15 min) and crude membranes were collected by ultracentrifugation (Ti45 rotor, 40000 rpm, 1 hour). The membranes were mechanically homogenized by pipetting and subsequently solubilized for 2 hours in a buffer containing 150 mM NaCl, 20 mM Tris-HCl (pH 8.0) and 20 mM $C_{12}M$ (*n*-dodecyl-β-D-maltopyranoside; 0.25 g of $C_{12}M$ / 1 g membranes). Insoluble material was removed by ultracentrifugation (Ti45 rotor, 40000 rpm, 40 min) and Strep-Tactin resin (0.5-1.0 ml per liter of cells) was added to the supernatant. After binding for 3-18 hours, the protein was eluted with the buffer containing 150 mM NaCl, 20 mM Tris-HCl (pH 8.0), 1 mM $C_{12}M$, and 2.5 mM desthiobiotin. Following concentration, the protein was first treated with EndoH (1:1 mass ratio of EndoH to receptor, 24 hours at 4°C), then digested with thrombin (1:200 mass ratio of thrombin to receptor, 1 hour at 22°C) and loaded onto a size exclusion chromatography (SEC) Superose 6 column equilibrated in a buffer composed of 150 mM NaCl, 20 mM Tris-HCl (pH 8.0), 1 mM *n*-undecyl-β-D-thiomaltopyranoside (C_{11}Thio) and 0.01 mg/ml lipid – 3:1:1 POPC:POPE:POPG (1-palmitoyl-2-oleoyl-sn-glycero-3-phosphocholine: 1-palmitoyl-2-oleoyl-sn-glycero-3-phosphoethanolamine, and 1-palmitoyl-2-oleoyl-sn-glycero-3-[phospho-rac-(1-glycerol)]). Peak fractions were pooled and concentrated to ~2 mg/ml for protein crystallization. All steps were performed at 4°C unless otherwise noted.

2.3 Crystallization and cryoprotection

The best crystals of the $GluA2_{Del}$ construct grew at 4°C in the hanging drop configuration. Prior to crystallization experiments, 2 mM 4-BCCA was added to the $GluA2_{Del}$ protein, which was then subjected to ultracentrifugation (Ti100 rotor, 40000 rpm, 40 min, 4°C). The protein solution was then mixed with a crystallization buffer at receptor to crystallization buffer ratio of 2:1. The best crystals grew in two conditions, when crystallization buffer was composed of 8-11% (w/v) PEG 8,000, 0.2 M magnesium acetate and 0.1 M sodium cacodylate (pH 6.3-6.7) or 11-14% (w/v) PEG 6,000, 0.1 M ammonium phosphate and 0.1 M TRIS (pH 7.9-8.0). Crystals appeared after 5-7 days, grew as bars and reached the maximal size (~100 μm × ~100 μm × ~300 μm) in 30-60 days. Cryoprotection was carried out at 4°C by serial transfer into buffers containing increasing concentrations of glycerol, up to the maximum concentration of 20% (v/v), and then plunged into liquid nitrogen.

2.4 Structure determination and analysis

X-ray diffraction data collected at the Advanced Photon Source (beamlines 24-ID-C/E) were indexed, integrated and scaled using XDS (Kabsch, 2010) or HKL2000 (Otwinowski & Minor, 1997) (Table 1). The structure of GluA2 in complex with 4-BCCA ($GluA2_{4\text{-}BCCA}$) was solved by molecular replacement using Phaser (McCoy, 2007) and the apo state $GluA2_{Del}$ structure (PDB ID: 5L1B) (Yelshanskaya, Singh, Sampson, Narangoda, Kurnikova & Sobolevsky, 2016) as a search probe. All structures were iteratively built in Coot (Emsley & Cowtan, 2004) and refined using Phenix (Adams et al., 2002). The four subunits in the tetrameric receptor structures contain residues 10 to 817, *N*-linked carbohydrates at N355 and molecules of 4-BCCA bound in the TMD. Regions with poor or missing electron density – residues in the M1-M2 loop (R545 to G572), in the non-helical region of M2 (A589 to R594) and in the carboxyl-terminus (K817 to G832) – were presumably disordered and therefore excluded from the final models. Structures were superposed using the CCP4 suite program Superpose (Krissinel &

Henrick, 2004). Structural illustrations were made using the PyMOL Molecular Graphics System (Schrodinger, LLC) (DeLano, 2002).

2.5 Electrophysiology

DNA encoding wild type or mutant GluA2 was introduced into a plasmid for expression in eukaryotic cells that was engineered to produce green fluorescent protein via a downstream internal ribosome entry site (Yelshanskaya, Singh, Sampson, Narangoda, Kurnikova & Sobolevsky, 2016). All mutations were made in wild type GluA2 background. Human embryonic kidney HEK293 cells grown on glass coverslips in 35-mm dishes were transiently transfected with 1-5 μg of plasmid DNA using Lipofectamine 2000 Reagent (Invitrogen). Recordings were made 24 to 72 hours after transfection at room temperature. Currents from whole cells or outside-out patches, typically held at a –60 mV potential, were recorded using Axopatch 200B amplifier (Molecular Devices, LLC), filtered at 5 kHz and digitized at 10 kHz using low-noise data acquisition system Digidata 1440A and pCLAMP software (Molecular Devices, LLC). The external solution contained (in mM): 140 NaCl, 2.4 KCl, 4 $CaCl_2$, 4 $MgCl_2$, 10 HEPES (pH 7.3) and 10 glucose; 7 mM NaCl was added to the extracellular activating solution containing 3 mM L-glutamate (Glu). The internal solution contained (in mM): 150 CsF, 10 NaCl, 10 EGTA, 20 HEPES (pH 7.3). Rapid solution exchange was achieved with a two-barrel theta glass pipette controlled by a piezoelectric translator. Typical 10-90% rise times were 200-300 μs, as measured from junction potentials at the open tip of the patch pipette after recordings. Data analysis was performed using the computer program Origin 9.1.0 (OriginLab Corp.).

2.6 Molecular Modelling

The TMD and the TMD-LBD linkers (residues 506-544, 573-632, 782-816) of the receptor were used as the starting structure for all simulations. Residues 545-572 were modelled in ModLoop webserver (Fiser & Sali, 2003) and all other missing atoms were added in tleap

program in AMBER16 MD simulation software package (Case et al., 2016). The receptor was embedded in a pre-equilibrated POPC lipid membrane and solvated in TIP3P water and neutralizing K^+ ions. Each simulated system consisted approximately of $98x10^3$ atoms, including 648 protein residues, either two or four 4-BCCA ligands, 240 POPC lipids, and approximately 18,600 waters and neutralizing ions. The topology and parameter files for charged and uncharged 4-BCCA were created using Antechamber package (Wang, Wang, Kollman & Case, 2001) and General AMBER force field (GAFF) (Wang, Wolf, Caldwell, Kollman & Case, 2004). All MD simulations were carried out using pmemd.cuda in AMBER16 (Case et al., 2016), using ff14SB force field (Maier, Martinez, Kasavajhala, Wickstrom, Hauser & Simmerling, 2015) in combination with GAFF (Wang, Wolf, Caldwell, Kollman & Case, 2004) and Lipid14 (Dickson et al., 2014) force fields. The simulation time step was 2 fs and all covalent bonds to hydrogen atoms were constrained via SHAKE (Dickson et al., 2014). Electrostatic interaction calculations were performed using Particle Mesh Ewald (PME) method (Darden, York & Pedersen, 1993). Periodic boundary conditions were applied in all directions with a cutoff radius of 10 Å. The Langevin thermostat was used to control temperature and the Berendsen barostat with anisotropic pressure scaling was used to maintain pressure. All equilibration and production simulations were carried out at 1 atm pressure and 300K temperature.

Each system was minimized for 50,000 steps prior to MD simulations. The system was heated to 100K at the constant volume and brought up to 300K at the constant pressure. Heating was carried out in five 50 ps steps, with protein Cα atoms and ligand heavy atoms restrained using a harmonic potential with the force constant of 20 kcal $mol^{-1}Å^{-2}$. The system was then equilibrated at a constant pressure for 12 ns during which the restraints on protein Cα atoms and ligands were gradually decreased from 20 to 0.1 kcal $mol^{-1}Å^{-2}$. During the final 5 ns of this step, only protein Cα atoms and ring carbons of 4-BCCA were restrained. Then all

restraints on ligands and protein were removed and the final equilibration step lasted 20 ns. Production simulations were carried out for 200 ns.

Post-processing of trajectories was done using cpptraj (Roe & Cheatham III, 2013) and VMD (Humphrey, Dalke & Schulten, 1996). Hydrogen bond analysis was carried out in cpptraj (Roe & Cheatham III, 2013) using the distance cut-off of 3.6 Å and angle cut-off of 135°. Protein-ligand contacts analysis and ligand density calculations were performed in VMD (Humphrey, Dalke & Schulten, 1996). Ligand RMSD was computed for heavy atoms of the ligand with reference to their initial positions, with each frame of the trajectory aligned using the coordinates of protein Cα atoms for residues 602 to 626 in the M3 helix.

2.7 Data and statistical analysis

The data and statistical analysis comply with the recommendations of the *British Journal of Pharmacology* on experimental design and analysis in pharmacology (Curtis et al., 2015). The results are presented as mean ± SEM. Statistical analysis was undertaken only for studies where each group size was at least $n = 5$. We used t-Test for comparisons, with differences considered statistically significant when $P < 0.05$.

2.8 Materials

Trans-4-Butylcyclohexanecarboxylic Acid (4-BCCA) was provided by Tokyo Chemical Industry UK Ltd, B1136.

3. RESULTS

3.1 Structure

To structurally characterize the interaction of 4-BCCA with AMPA receptors, we used a modified rat GluA2 subunit construct ($GluA2_{Del}$) that displays functional properties similar to wild type receptors and was used previously to solve structures of AMPA receptor in the apo state and in complex with noncompetitive inhibitors (Yelshanskaya, Singh, Sampson,

Narangoda, Kurnikova & Sobolevsky, 2016). Crystals of $GluA2_{Del}$ grew readily in the presence of 4-BCCA, belonged to the $P2_12_12_1$ space group with one tetramer per asymmetric unit and diffracted to 3.7-4.25 Å resolution. We solved the structure of GluA2 in complex with 4-BCCA ($GluA2_{4\text{-}BCCA}$) by molecular replacement using the apo state structure (PDB ID: 5L1B) as an initial search probe. The resulting electron density maps were of sufficient quality to build a molecular model of the entire receptor, excluding sections of the intracellular linkers connecting the transmembrane domain (TMD) segments M1 to M2 and M2 to M3, which were not visible in electron density maps, presumably due to their dynamic nature. The final model showed reliable crystallographic statistics and stereochemistry (Table 1).

$GluA2_{4\text{-}BCCA}$ structure has a typical AMPA receptor domain arrangement and the overall Y shape (Sobolevsky, Rosconi & Gouaux, 2009) (Figure 2a). A large extracellular domain (ECD) comprises the amino-terminal domain (ATD) layer that sits atop of the Y and is necessary for receptor assembly, trafficking and functional regulation (Ayalon & Stern-Bach, 2001; Traynelis et al., 2010) and the ligand binding domain (LBD) layer in the middle of Y, which harbours binding sites for ligands that activate, modulate or antagonize the receptor (Gouaux, 2004; Stern-Bach, Bettler, Hartley, Sheppard, O'Hara & Heinemann, 1994). Below the ATD and LBD layers is the transmembrane domain (TMD) (Figure 2b) that forms a cation-selective ion channel (Wollmuth & Sobolevsky, 2004). Each LBD is comprised of two polypeptide stretches, S1 and S2, which form a clamshell structure, with ligand binding occurring in the middle, between the LDB upper (D1) and lower (D2) lobes. The TMD includes three transmembrane helices (M1, M3 and M4) and a re-entrant intracellular loop M2 between helices M1 and M3. Each LBD is tethered to the TMD through flexible polypeptide linkers S1-M1, M3-S2, and S2-M4. These linkers communicate conformational changes in the LBD induced by ligand binding to the TMD (Twomey & Sobolevsky, 2018).

The Fo-Fc maps generated for about 30 complete crystallographic datasets collected from crystals of $GluA2_{Del}$ grown in the presence of 4-BCCA, with the maximum diffraction resolution between 3.7 and 4.25 Å, consistently showed positive densities in the TMD side portals located at the intersubunit interfaces and formed mainly by the M1 and M3 segments. These densities have not been previously observed in the apo-state, agonist-bound or noncompetitive inhibitor-bound structures (Yelshanskaya, Li & Sobolevsky, 2014; Yelshanskaya, Singh, Sampson, Narangoda, Kurnikova & Sobolevsky, 2016). The strength of these densities in $GluA2_{4\text{-}BCCA}$ varied between the datasets as well as between intersubunit interfaces, being on average stronger for one diagonal pair of interfaces, A-D and B-C, and weaker for another pair, A-B and C-D (Figure 2b-c), consistent with different structural and functional roles of the two pairs of diagonal subunits (Dong & Zhou, 2011; Kazi, Dai, Sweeney, Zhou & Wollmuth, 2014; Twomey, Yelshanskaya, Grassucci, Frank & Sobolevsky, 2017). The size and shape of these densities matched those of 4-BCCA molecules but the precise orientation of the 4-BCCA molecules fitting these densities was rather ambiguous due to relatively low resolution. The corresponding putative binding sites of 4-BCCA are surrounded by mostly hydrophobic residues of M1 (L521, W526 and I529), M2 (F584, M585) and M3 (T609, I612, I613, Y616 and T617) of one subunit and M3 (F607, L610, I611 and S614) of the neighbouring subunit (Figure 2c).

3.2 MD simulations of 4-BCCA interaction with wild type AMPA receptors

To verify putative 4-BCCA binding sites identified by X-ray crystallography and to better understand the chemical nature of 4-BCCA interactions with AMPA receptor, we performed molecular dynamics (MD) simulations. First, we constructed a model of the GluA2 receptor transmembrane domain based on the crystal structure (see Methods). The protein model was embedded into a POPC lipid bilayer surrounded by water and ions (Figure 3a). The entire model system was equilibrated using the previously developed protocol (Narangoda, Sakipov

& Kurnikova, 2019). Parameters for 4-BCCA model molecule were specifically developed for this study. In addition to the crystal structure with two 4-BCCA molecules at A-D and B-C subunit interfaces, two complexes were created by inserting 4-BCCA into all four equivalent binding sites of the protein in each of the two conformations in the crystal structure. Each system was simulated in both protonated and deprotonated states of the carboxylate group of 4-BCCA, resulting in six simulations of the wild type protein containing a total of twenty 4-BCCA ligands. On average, 4-BCCA molecules remained in close proximity to their initial positions but were mobile and exhibited significant reorientation during simulations, illustrated by representative positions of 4-BCCA from all simulations (Figure 3b) and combined density of the ligand averaged over all simulations (Figure 3c). As expected, deprotonated 4-BCCA entered the channel pore more readily than protonated 4-BCCA (Figure 3b). Three deprotonated ligands escaped the binding site and moved towards the pre-M1 and TMD-LBD linkers. Nevertheless, the region of the highest ligand density in simulations clearly coincides with the 4-BCCA position resolved by X-ray crystallography (Figure 3c). Consistent with the crystal structure (Figure 2c), the majority of simulated ligands formed contacts with residues of M1 (W526, I529), M2 (F584), and M3 (I612, I613, Y616, T617) of one subunit and M3 (F607, L610, I611, S614) of the neighbouring subunit (Figure 3c).

Interestingly, the average position of 4-BCCA in MD simulations is immediately adjacent to the preferred positions of lipid molecules in the vicinity of the 4-BCCA binding site. In MD simulations, residues W526 and F607, and sometimes I529 and F584, are in contact with membrane lipids (Supplementary Table 1). In the absence of 4-BCCA (or when 4-BCCA shifts away from its average binding position), lipids tend to form contacts with additional residues of the M3 helices that form the binding pocket (Supplementary Table 1). In simulations of AMPA receptors with noncompetitive inhibitors PMP, GYKI, and CP, which bind to a different site in the extracellular collar of the receptor, lipids interacted with M585 in addition

to the residues mentioned above. Figure 3d shows the overlap in the positions of ligand density in 4-BCCA simulations and membrane lipids in a simulation of GluA2 in the absence of 4-BCCA. We hypothesize that the mechanism of AMPA receptor inhibition by 4-BCCA may involve destabilization of the protein surface by 4-BCCA outcompeting some of the annular lipids.

3.3 Probing of 4-BCCA binding sites by mutagenesis and electrophysiology

To functionally verify the putative binding sites, we mutated several residues in close proximity to the presumed 4-BCCA location and used the whole-cell patch-clamp technique to record currents from wild type and mutant AMPA receptors expressed in HEK 293 cells (Figure 4). Wild type GluA2 receptors were weakly inhibited by 4-BCCA showing only 40 ± 4 % current inhibition in response to 2 mM 4-BCCA application (Figure 4a). About half of the GluA2 mutants did not show any measurable current (Figure 4b), consistent with the location of the putative 4-BCCA binding sites right next to the ion channel activation gate formed by T617, A621, T625 and M629 at the M3 bundle crossing (Sobolevsky, Rosconi & Gouaux, 2009; Twomey & Sobolevsky, 2018; Twomey, Yelshanskaya, Grassucci, Frank & Sobolevsky, 2017). Indeed, many previous studies showed that mutations in this region of iGluR often result in leaky or non-functional receptors or receptors with severely altered kinetics (Beck, Wollmuth, Seeburg, Sakmann & Kuner, 1999; Chang & Kuo, 2008; Jones, VanDongen & VanDongen, 2002; Kashiwagi et al., 2002; Kohda, Wang & Yuzaki, 2000; Sobolevsky, Prodromou, Yelshansky & Wollmuth, 2007; Sobolevsky, Yelshansky & Wollmuth, 2003).

For those mutants that did show currents in response to glutamate application, we observed three types of effects: (1) no change in 4-BCCA inhibition (e.g., L610F and S614Q, Figure 4b), (2) reduced inhibition (e.g., M585A, Figure 4a) and (3) increased inhibition (e.g., S614L, Figure 4a). To better understand possible reasons for such effects, we performed MD

simulations of the mutant receptors and compared the results with those for the wild type receptors.

3.4 MD simulations of 4-BCCA interaction with mutant AMPA receptors

We have performed MD simulations of the mutants L610F, S614L, S614N, S614Q, M585A, and M585Q in complex with four protonated 4-BCCA molecules. In these simulations of mutant AMPA receptors, 4-BCCA exhibited two distinct changes in the behaviour compared to wild type receptors. In S614N and S614Q mutants, the 4-BCCA ligands interacted strongly with the mutated residues as most of them formed a hydrogen bond with the side chain amide group (Figure 5a and Table 2). In both S614N and S614Q mutant receptors, one of the ligands had entered the ion channel (Figure 5b). Formation of a hydrogen bond between the side chain of S614 and 4-BCCA was also observed in simulations of wild type GluA2. However, the protonated ligands in simulations of wild type receptors tended to remain at their binding sites. The lack of the hydrogen bond in the S614L mutant resulted in reduced interaction between 4-BCCA and leucine at position 614 and fewer contacts of 4-BCCA with I611 and I613 as well (Figure 5c and Table 2). In contrast to the S614N and S614Q mutants, the 4-BCCA ligands in S614L receptors tended to shift away from the ion channel pore toward the membrane lipids. Phenylalanine substitution in the L610F receptors also resulted in reduced interactions between 4-BCCA and residues S614, I611, and I613 (Figure 5d and Table 2). Although the ligands in L610F and S614L mutant receptors did not enter the ion channel pore, they interacted more extensively with the adjacent to the selectivity filter residues F584 and M585 (Figure 5d). In M585W and M585A receptors, the 4-BCCA ligands did not interact significantly with the mutated residues although one ligand in the M585W receptor had entered the ion channel pore. Overall, those molecules of 4-BCCA that had entered the pore also interacted with the residues at positions 614 and/or 610 of multiple subunits, as illustrated in Figure 5b. We also observed changes in the selectivity filter stability. For example, much lower flexibility of the selectivity

filter and the entire M2 segment was observed in simulations of the S614N mutant compared to wild type receptors, signifying an improvement of the overall protein stability.

The reduced current inhibition observed for the M585A mutant (Figure 4) could be due to reduced hydrophobicity of the side portal that leads to the putative 4-BCCA binding site, which might be necessary for the inhibitor entry. On the contrary, the weakly reduced inhibition observed for the M585W mutant could be due to the bulky indole ring of tryptophan physically obstructing the access of 4-BCCA to its binding site but this effect, if present, is insignificant. MD results do not contradict the experimental results because the simulations started with 4-BCCA already at the binding site. In M585A and M585W, ligands did not interact with the mutated residue. In M585W, one ligand entered the pore. In case of S614 mutations, different substitutions produced different effects, suggesting that the size, hydrophobicity and possibly the exact chemical character of the substituent side chain affects 4-BCCA inhibition. Thus, substitution of the hydroxymethyl group of serine with the amide group of asparagine in the S614N mutant resulted in significantly reduced current inhibition (Figure 4b), possibly due to the altered chemical microenvironment that is important for 4-BCCA binding. Our MD simulations also showed that the selectivity filter is less flexible in the S614N mutant compared to the S614Q mutant and wild type protein, probably reflecting the altered protein dynamics in the presence of 4-BCCA.

Interestingly, in case of the S614Q mutant, an increase in the size of the substituent side chain, which also has the amide group, almost entirely eliminated the reduction of inhibition observed for the S614N mutant, indicating an importance of the side chain size. On the other hand, substitution of the hydroxymethyl group of serine with the bulkier isobutyl group of leucine in the S614L mutant resulted in increased current inhibition, suggesting the importance of local hydrophobicity for 4-BCCA binding. In MD simulations of the S614L mutant, the loss of hydrogen bond between residue 614 and the ligand also resulted in reduced interactions

between 4-BCCA and residues I611 and I613. No ligands entered the channel pore but 4-BCCA interacted with the adjacent to the selectivity filter residues F584 and M585 more extensively. Simulations of L610F, which showed no significant change in current inhibition (Figure 4b), gave similar results. At the same time, the majority of ligands in simulations of S614L moved away from the pore and interacted with lipids slightly more compared to other mutants. Overall, the results of our MD simulations and electrophysiological experiments on mutant and wild type receptors support the location of 4-BCCA binding sites identified crystallographically and provide clues about the mechanism of AMPA receptor inhibition by 4-BCCA.

4. DISCUSSION AND CONCLUSIONS

4.1 Unique 4-BCCA binding site and mechanism of AMPA receptor regulation

Using X-ray crystallography, we identified binding sites of 4-BCCA in the TMD of GluA2 AMPA receptor. These sites are located in the intramembranous side portals between transmembrane segments M1-M4, which connect the interior of the lipid bilayer to the ion channel pore, and are mostly contributed by residues in M1 and M3 (Figure 2). The 4-BCCA molecules are highly dynamic at their binding sites, assume different poses and occasionally enter the ion channel pore or the extracellular collar cavities between the pre-M1 and M3 segments (Figure 3). The dynamic character of 4-BCCA molecules bound to AMPA receptor and the approximate location of their binding sites were supported by mutagenesis combined with electrophysiology (Figure 4) and by MD simulations of mutant receptors (Figure 5). The dynamics of 4-BCCA is consistent with its low affinity towards GluA2 (Figure 4), which has been shown to be ~5 fold lower than towards GluA3 (Chang et al., 2015), and is a likely reason for the lack of markers indicating possible detrimental developmental and neurological side effects (Chang et al., 2015) that are typical for AEDs (Coyle, Clough, Cooper & Mohanraj, 2014; Rugg-Gunn, 2014; Steinhoff et al., 2014).

The location of 4-BCCA binding sites suggests possible molecular mechanisms of AMPA receptor inhibition. We hypothesize that 4-BCCA inhibits AMPA receptor by either making its presence at the ion channel pore and directly interfering with the flow of permeant ions (Figure 3b), or rigidifying the dynamics of the M3 segments, kinking of which is necessary for the channel to open (Twomey & Sobolevsky, 2018; Twomey, Yelshanskaya, Grassucci, Frank & Sobolevsky, 2017), or destabilizing the protein surface through competition with the surrounding membrane lipids (Figure 3d). It remains unclear how 4-BCCA molecules reach their binding sites. Being hydrophobic, 4-BCCA molecules can enter the ion channel side portals by going through the membrane but reaching the same sites by going through the pore cannot be excluded either, which would be consistent with 4-BCCA molecules entering the pore in MD simulations (Figure 3) and inhibiting currents in the presence of Glu in electrophysiological experiments (Figure 4). The identified 4-BCCA binding sites are likely locations for the whole cohort of the MCT ketogenic diet-associated medium chain fatty acids and their branched derivatives that share the inhibitory mechanism and represent promising AEDs (Chang et al., 2016; Chang et al., 2015). iGluRs are also modulated by polyunsaturated fatty acids, like docosahexanoic acid (DHA) and arachidonic acid (Miller, Sarantis, Traynelis & Attwell, 1992; Wilding, Chai & Huettner, 1998). Mutations of residues M589 and S618 in GluK2, homologous to residues M585 and S614 in GluA2 that affect 4-BCCA binding (Figure 4), produced strong effects on regulation of kainate receptors by DHA (Wilding, Chen & Huettner, 2010; Wilding, Fulling, Zhou & Huettner, 2008), suggesting that some of the effects of polyunsaturated fatty acids on iGluRs might be due to their binding to the 4-BCCA sites. Future studies will be required to examine this possibility in detail.

4.2 Synergy with other TMD regulators of AMPA receptor and clinical relevance

Interestingly, 4-BCCA binding sites are located in close proximity to the extracellular collar binding sites of noncompetitive inhibitors, including AED PMP (Figure 6). While our MD

simulations suggest a possibility that such close proximity might result in 4-BCCA molecules occasionally approaching noncompetitive inhibitor binding sites, most of the time they stay away from these sites. There is therefore a strong possibility of simultaneous binding of 4-BCCA and PMP to AMPA receptor, which explains the synergy between these molecules observed in rodent and human brain slice experiments (Augustin et al., 2018b).

The dynamic character of 4-BCCA revealed by MD simulations also suggests that this molecule can periodically enter the ion channel pore (Figure 3). In calcium-permeable AMPA receptors (which have glutamine at the Q/R-site, like the receptors in the present study), the ion channel pore is a binding site for blockers, which include endogenous polyamines, such as spermine and spermidine (Bowie & Mayer, 1995; Donevan & Rogawski, 1995; Kamboj, Swanson & Cull-Candy, 1995; Koh, Burnashev & Jonas, 1995), as well as exogenous polyamine- or acylpolyamine-containing toxins, such as philanthotoxin-433 from the wasp *Philanthus triangulum* (Eldefrawi et al., 1988), argiotoxin-636 from the spider *Argiope lobata* (Antonov, Grishin, Magazanik, Shupliakov, Vesselkin & Volkova, 1987; Grishin, Volkova, Arsen'ev, Reshetova & Onoprienko, 1986), Joro spider toxin JSTX-3 from *Nephilia clavata* (Aramaki, Yasuhara, Shimazaki, Kawai & Nakajima, 1987) and its synthetic analogue 1-naphthyl acetyl spermine (NASPM) (Koike, Iino & Ozawa, 1997; Takazawa, Yamazaki, Kanai, Ishida, Kato & Yamauchi, 1996; Twomey, Yelshanskaya, Vassilevski & Sobolevsky, 2018) (Figure 6). Since excessive activity of calcium-permeable AMPA receptors results in increased neuronal oxidative stress, which leads to cell damage and degeneration (Carriedo, Sensi, Yin & Weiss, 2000; Carriedo, Yin, Sensi & Weiss, 1998; Carriedo, Yin & Weiss, 1996; Weiss, 2011), calcium-permeable AMPA receptors have been linked to neurological disorders, including amyotrophic lateral sclerosis (Carriedo, Sensi, Yin & Weiss, 2000; Selvaraj et al., 2018; Tateno et al., 2004; Van Damme, Braeken, Callewaert, Robberecht & Van Den Bosch, 2005), Alzheimer's (Whitehead, Regan, Whitcomb & Cho, 2017) and Parkinson's (Kobylecki,

Cenci, Crossman & Ravenscroft, 2010) diseases, ischemia-induced neuronal cell death (Liu et al., 2004; Talos et al., 2006; Yin, Hsu, Yu, Rao, Sorkin & Weiss, 2012) and epilepsy (Lippman-Bell, Zhou, Sun, Feske & Jensen, 2016; Rajasekaran, Todorovic & Kapur, 2012; Rogawski, 2013). Calcium-permeable AMPA receptors have also been associated with increased sensitivity to pain and hyperalgesia (Gangadharan et al., 2011; Park et al., 2009; Sullivan, Farrant & Cull-Candy, 2017), addiction (Mameli, Bellone, Brown & Luscher, 2011; Schmidt et al., 2015) and development of glaucoma (Cueva Vargas et al., 2015). In addition, calcium-permeable AMPA receptors have been recently shown to cause an increase in glioma cell intracellular calcium and brain tumour progression (Venkataramani et al., 2019; Venkatesh et al., 2019), while their elevated expression during development contributed to abnormal CNS development and fragile-X syndrome (Achuta et al., 2018).

All three classes of molecules binding at the TMD of AMPA receptor (Figure 6) are therefore promising candidates for the development of therapeutics targeting a broad spectrum of neurological disorders and brain tumours. Due to the distinct binding sites for all three compounds, they are likely to simultaneously bind to AMPA receptor, resulting in synergetic inhibition of the receptor, as it was demonstrated for DA and PMP (Augustin et al., 2018b). Thus, co-administration of representatives of these three classes of molecules might provide a future strategy for the treatment of neurological disorders and gliomas.

REFERENCES

Achuta VS, Moykkynen T, Peteri UK, Turconi G, Rivera C, Keinanen K, *et al.* (2018). Functional changes of AMPA responses in human induced pluripotent stem cell-derived neural progenitors in fragile X syndrome. Science signaling 11.

Adams PD, Grosse-Kunstleve RW, Hung LW, Ioerger TR, McCoy AJ, Moriarty NW, *et al.* (2002). PHENIX: building new software for automated crystallographic structure determination. Acta Crystallogr D Biol Crystallogr 58**:** 1948-1954.

Alsdorf R, & Wyszynski DF (2005). Teratogenicity of sodium valproate. Expert Opin Drug Saf 4**:** 345-353.

Antonov SM, Grishin EV, Magazanik LG, Shupliakov OV, Vesselkin NP, & Volkova TM (1987). Argiopin blocks the glutamate responses and sensorimotor transmission in motoneurones of isolated frog spinal cord. Neurosci Lett 83**:** 179-184.

Aramaki Y, Yasuhara T, Shimazaki K, Kawai N, & Nakajima T (1987). Chemical structure of Joro spider toxin (JSTX). Biomedical Research 8**:** 241-245.

Augustin K, Khabbush A, Williams S, Eaton S, Orford M, Cross JH, *et al.* (2018a). Mechanisms of action for the medium-chain triglyceride ketogenic diet in neurological and metabolic disorders. Lancet Neurol 17**:** 84-93.

Augustin K, Williams S, Cunningham M, Devlin AM, Friedrich M, Jayasekera A, *et al.* (2018b). Perampanel and decanoic acid show synergistic action against AMPA receptors and seizures. Epilepsia 59**:** e172-e178.

Ayalon G, & Stern-Bach Y (2001). Functional assembly of AMPA and kainate receptors is mediated by several discrete protein-protein interactions. Neuron 31**:** 103-113.

Barker-Haliski M (2019). How do we choose the appropriate animal model for antiseizure therapy development? Expert Opin Drug Discov 14**:** 947-951.

Beck C, Wollmuth LP, Seeburg PH, Sakmann B, & Kuner T (1999). NMDAR channel segments forming the extracellular vestibule inferred from the accessibility of substituted cysteines. Neuron 22**:** 559-570.

Bough KJ, & Rho JM (2007). Anticonvulsant mechanisms of the ketogenic diet. Epilepsia 48**:** 43-58.

Bowie D, & Mayer ML (1995). Inward rectification of both AMPA and kainate subtype glutamate receptors generated by polyamine-mediated ion channel block. Neuron 15**:** 453-462.

Burnashev N, Monyer H, Seeburg PH, & Sakmann B (1992). Divalent ion permeability of AMPA receptor channels is dominated by the edited form of a single subunit. Neuron 8**:** 189-198.

Carriedo SG, Sensi SL, Yin HZ, & Weiss JH (2000). AMPA exposures induce mitochondrial Ca(2+) overload and ROS generation in spinal motor neurons in vitro. The Journal of neuroscience : the official journal of the Society for Neuroscience 20**:** 240-250.

Carriedo SG, Yin HZ, Sensi SL, & Weiss JH (1998). Rapid Ca2+ entry through Ca2+-permeable AMPA/Kainate channels triggers marked intracellular Ca2+ rises and consequent oxygen radical production. The Journal of neuroscience : the official journal of the Society for Neuroscience 18**:** 7727-7738.

Carriedo SG, Yin HZ, & Weiss JH (1996). Motor neurons are selectively vulnerable to AMPA/kainate receptor-mediated injury in vitro. The Journal of neuroscience : the official journal of the Society for Neuroscience 16**:** 4069-4079.

Case D, Cerutti D, Cheateham T, Darden T, Duke R, Giese T, *et al.* (2016). AMBER16 Package. University of California, San Francisco.

Chang HR, & Kuo CC (2008). The activation gate and gating mechanism of the NMDA receptor. J Neurosci 28**:** 1546-1556.

Chang P, Augustin K, Boddum K, Williams S, Sun M, Terschak JA, *et al.* (2016). Seizure control by decanoic acid through direct AMPA receptor inhibition. Brain 139**:** 431-443.

Chang P, Orabi B, Deranieh RM, Dham M, Hoeller O, Shimshoni JA, *et al.* (2012). The antiepileptic drug valproic acid and other medium-chain fatty acids acutely reduce phosphoinositide levels independently of inositol in Dictyostelium. Dis Model Mech 5**:** 115-124.

Chang P, Terbach N, Plant N, Chen PE, Walker MC, & Williams RS (2013). Seizure control by ketogenic diet-associated medium chain fatty acids. Neuropharmacology 69**:** 105-114.

Chang P, Walker MC, & Williams RS (2014). Seizure-induced reduction in PIP3 levels contributes to seizure-activity and is rescued by valproic acid. Neurobiol Dis 62**:** 296-306.

Chang P, Zuckermann AM, Williams S, Close AJ, Cano-Jaimez M, McEvoy JP, *et al.* (2015). Seizure control by derivatives of medium chain fatty acids associated with the ketogenic diet show novel branching-point structure for enhanced potency. J Pharmacol Exp Ther 352**:** 43-52.

Cormack BP, Valdivia RH, & Falkow S (1996). FACS-optimized mutants of the green fluorescent protein (GFP). Gene 173**:** 33-38.

Coyle H, Clough P, Cooper P, & Mohanraj R (2014). Clinical experience with perampanel: focus on psychiatric adverse effects. Epilepsy Behav 41**:** 193-196.

Cueva Vargas JL, Osswald IK, Unsain N, Aurousseau MR, Barker PA, Bowie D, *et al.* (2015). Soluble Tumor Necrosis Factor Alpha Promotes Retinal Ganglion Cell Death in Glaucoma via Calcium-Permeable AMPA Receptor Activation. The Journal of neuroscience : the official journal of the Society for Neuroscience 35**:** 12088-12102.

Curtis MJ, Bond RA, Spina D, Ahluwalia A, Alexander SP, Giembycz MA, *et al.* (2015). Experimental design and analysis and their reporting: new guidance for publication in BJP. Br J Pharmacol 172**:** 3461-3471.

Darden T, York D, & Pedersen L (1993). Particle mesh Ewald: An N· log (N) method for Ewald sums in large systems. The Journal of chemical physics 98**:** 10089-10092.

DeLano WL (2002). The PyMOL Molecular Graphics SystemDeLano Scientific: San Carlos, CA, USA.

Dickson CJ, Madej BD, Skjevik ÅA, Betz RM, Teigen K, Gould IR, *et al.* (2014). Lipid14: the amber lipid force field. Journal of chemical theory and computation 10**:** 865-879.

Donevan SD, & Rogawski MA (1995). Intracellular polyamines mediate inward rectification of Ca(2+)-permeable alpha-amino-3-hydroxy-5-methyl-4-isoxazolepropionic acid receptors. Proc Natl Acad Sci U S A 92**:** 9298-9302.

Dong H, & Zhou HX (2011). Atomistic mechanism for the activation and desensitization of an AMPA-subtype glutamate receptor. Nat Commun 2**:** 354.

Eldefrawi AT, Eldefrawi ME, Konno K, Mansour NA, Nakanishi K, Oltz E, *et al.* (1988). Structure and synthesis of a potent glutamate receptor antagonist in wasp venom. Proceedings of the National Academy of Sciences of the United States of America 85**:** 4910-4913.

Emsley P, & Cowtan K (2004). Coot: model-building tools for molecular graphics. Acta Crystallogr D Biol Crystallogr 60**:** 2126-2132.

Fiser A, & Sali A (2003). ModLoop: automated modeling of loops in protein structures. Bioinformatics 19**:** 2500-2501.

Frampton JE (2015). Perampanel: A Review in Drug-Resistant Epilepsy. Drugs 75**:** 1657-1668.

Gangadharan V, Wang R, Ulzhofer B, Luo C, Bardoni R, Bali KK, *et al.* (2011). Peripheral calcium-permeable AMPA receptors regulate chronic inflammatory pain in mice. The Journal of clinical investigation 121**:** 1608-1623.

Goehring A, Lee CH, Wang KH, Michel JC, Claxton DP, Baconguis I, *et al.* (2014). Screening and large-scale expression of membrane proteins in mammalian cells for structural studies. Nat Protoc 9**:** 2574-2585.

Gottlicher M, Minucci S, Zhu P, Kramer OH, Schimpf A, Giavara S, *et al.* (2001). Valproic acid defines a novel class of HDAC inhibitors inducing differentiation of transformed cells. EMBO J 20**:** 6969-6978.

Gouaux E (2004). Structure and function of AMPA receptors. The Journal of physiology 554**:** 249-253.

Grishin EV, Volkova TM, Arsen'ev AS, Reshetova OS, & Onoprienko VV (1986). [Structural-functional characteristics of argiopine--the ion channel blockers from the spider Argiope lobata venom]. Bioorg Khim 12**:** 1121-1124.

Gurvich N, Tsygankova OM, Meinkoth JL, & Klein PS (2004). Histone deacetylase is a target of valproic acid-mediated cellular differentiation. Cancer Res 64**:** 1079-1086.

Hollmann M, O'Shea-Greenfield A, Rogers SW, & Heinemann S (1989). Cloning by functional expression of a member of the glutamate receptor family. Nature 342**:** 643-648.

Hume RI, Dingledine R, & Heinemann SF (1991). Identification of a site in glutamate receptor subunits that controls calcium permeability. Science 253**:** 1028-1031.

Humphrey W, Dalke A, & Schulten K (1996). VMD: visual molecular dynamics. Journal of molecular graphics 14**:** 33-38.

Jones KS, VanDongen HM, & VanDongen AM (2002). The NMDA receptor M3 segment is a conserved transduction element coupling ligand binding to channel opening. J Neurosci 22**:** 2044-2053.

Kabsch W (2010). Xds. Acta Crystallogr D Biol Crystallogr 66**:** 125-132.

Kamboj SK, Swanson GT, & Cull-Candy SG (1995). Intracellular spermine confers rectification on rat calcium-permeable AMPA and kainate receptors. J Physiol 486**:** 297-303.

Kashiwagi K, Masuko T, Nguyen CD, Kuno T, Tanaka I, Igarashi K, *et al.* (2002). Channel blockers acting at N-methyl-D-aspartate receptors: differential effects of mutations in the vestibule and ion channel pore. Mol Pharmacol 61**:** 533-545.

Kazi R, Dai J, Sweeney C, Zhou HX, & Wollmuth LP (2014). Mechanical coupling maintains the fidelity of NMDA receptor-mediated currents. Nat Neurosci 17**:** 914-922.

Keinänen K, Wisden W, Sommer B, Werner P, Herb A, Verdoorn TA, *et al.* (1990). A family of AMPA-selective glutamate receptors. Science 249**:** 556-560.

Kobylecki C, Cenci MA, Crossman AR, & Ravenscroft P (2010). Calcium-permeable AMPA receptors are involved in the induction and expression of l-DOPA-induced dyskinesia in Parkinson's disease. Journal of neurochemistry 114**:** 499-511.

Koh DS, Burnashev N, & Jonas P (1995). Block of native Ca(2+)-permeable AMPA receptors in rat brain by intracellular polyamines generates double rectification. J Physiol 486**:** 305-312.

Kohda K, Wang Y, & Yuzaki M (2000). Mutation of a glutamate receptor motif reveals its role in gating and delta2 receptor channel properties. Nat Neurosci 3**:** 315-322.

Koike M, Iino M, & Ozawa S (1997). Blocking effect of 1-naphthyl acetyl spermine on Ca(2+)-permeable AMPA receptors in cultured rat hippocampal neurons. Neuroscience research 29**:** 27-36.

Krissinel E, & Henrick K (2004). Secondary-structure matching (SSM), a new tool for fast protein structure alignment in three dimensions. Acta Crystallogr D Biol Crystallogr 60**:** 2256-2268.

Lippman-Bell JJ, Zhou C, Sun H, Feske JS, & Jensen FE (2016). Early-life seizures alter synaptic calcium-permeable AMPA receptor function and plasticity. Molecular and cellular neurosciences 76**:** 11-20.

Liu S, Lau L, Wei J, Zhu D, Zou S, Sun HS, *et al.* (2004). Expression of Ca(2+)-permeable AMPA receptor channels primes cell death in transient forebrain ischemia. Neuron 43**:** 43-55.

Maier JA, Martinez C, Kasavajhala K, Wickstrom L, Hauser KE, & Simmerling C (2015). ff14SB: improving the accuracy of protein side chain and backbone parameters from ff99SB. Journal of chemical theory and computation 11**:** 3696-3713.

Mameli M, Bellone C, Brown MT, & Luscher C (2011). Cocaine inverts rules for synaptic plasticity of glutamate transmission in the ventral tegmental area. Nature neuroscience 14**:** 414-416.

McCoy AJ (2007). Solving structures of protein complexes by molecular replacement with Phaser. Acta Crystallogr D Biol Crystallogr 63**:** 32-41.

Miller B, Sarantis M, Traynelis SF, & Attwell D (1992). Potentiation of NMDA receptor currents by arachidonic acid. Nature 355**:** 722-725.

Narangoda C, Sakipov SN, & Kurnikova MG (2019). AMPA Receptor Noncompetitive Inhibitors Occupy a Promiscuous Binding Site. ACS Chem Neurosci 10**:** 4511-4521.

Neal EG, Chaffe H, Schwartz RH, Lawson MS, Edwards N, Fitzsimmons G, *et al.* (2009). A randomized trial of classical and medium-chain triglyceride ketogenic diets in the treatment of childhood epilepsy. Epilepsia 50**:** 1109-1117.

Otwinowski Z, & Minor W (1997). Processing of X-ray diffraction data collected in oscillation mode. Methods Enzymol 276**:** 307-326.

Park JS, Voitenko N, Petralia RS, Guan X, Xu JT, Steinberg JP, *et al.* (2009). Persistent inflammation induces GluR2 internalization via NMDA receptor-triggered PKC activation in dorsal horn neurons. The Journal of neuroscience : the official journal of the Society for Neuroscience 29**:** 3206-3219.

Rajasekaran K, Todorovic M, & Kapur J (2012). Calcium-permeable AMPA receptors are expressed in a rodent model of status epilepticus. Annals of neurology 72**:** 91-102.

Roe DR, & Cheatham III TE (2013). PTRAJ and CPPTRAJ: software for processing and analysis of molecular dynamics trajectory data. Journal of chemical theory and computation 9**:** 3084-3095.

Rogawski MA (2011). Revisiting AMPA receptors as an antiepileptic drug target. Epilepsy Curr 11**:** 56-63.

Rogawski MA (2013). AMPA receptors as a molecular target in epilepsy therapy. Acta neurologica Scandinavica Supplementum**:** 9-18.

Rugg-Gunn F (2014). Adverse effects and safety profile of perampanel: a review of pooled data. Epilepsia 55 Suppl 1**:** 13-15.

Schmidt HD, McFarland KN, Darnell SB, Huizenga MN, Sangrey GR, Cha JH, *et al.* (2015). ADAR2-dependent GluA2 editing regulates cocaine seeking. Molecular psychiatry 20**:** 1460-1466.

Selvaraj BT, Livesey MR, Zhao C, Gregory JM, James OT, Cleary EM, *et al.* (2018). C9ORF72 repeat expansion causes vulnerability of motor neurons to Ca(2+)-permeable AMPA receptor-mediated excitotoxicity. Nature communications 9**:** 347.

Sobolevsky AI, Prodromou ML, Yelshansky MV, & Wollmuth LP (2007). Subunit-specific contribution of pore-forming domains to NMDA receptor channel structure and gating. J Gen Physiol 129**:** 509-525.

Sobolevsky AI, Rosconi MP, & Gouaux E (2009). X-ray structure, symmetry and mechanism of an AMPA-subtype glutamate receptor. Nature 462**:** 745-756.

Sobolevsky AI, Yelshansky MV, & Wollmuth LP (2003). Different gating mechanisms in glutamate receptor and K+ channels. J Neurosci 23**:** 7559-7568.

Sommer B, Kohler M, Sprengel R, & Seeburg PH (1991). RNA editing in brain controls a determinant of ion flow in glutamate-gated channels. Cell 67**:** 11-19.

Steinhoff BJ, Hamer H, Trinka E, Schulze-Bonhage A, Bien C, Mayer T, *et al.* (2014). A multicenter survey of clinical experiences with perampanel in real life in Germany and Austria. Epilepsy Res 108**:** 986-988.

Stern-Bach Y, Bettler B, Hartley M, Sheppard PO, O'Hara PJ, & Heinemann SF (1994). Agonist selectivity of glutamate receptors is specified by two domains structurally related to bacterial amino acid-binding proteins. Neuron 13**:** 1345-1357.

Sullivan SJ, Farrant M, & Cull-Candy SG (2017). TARP gamma-2 Is Required for Inflammation-Associated AMPA Receptor Plasticity within Lamina II of the Spinal Cord Dorsal Horn. The Journal of neuroscience : the official journal of the Society for Neuroscience 37**:** 6007-6020.

Takazawa A, Yamazaki O, Kanai H, Ishida N, Kato N, & Yamauchi T (1996). Potent and long-lasting anticonvulsant effects of 1-naphthylacetyl spermine, an analogue of Joro spider toxin, against amygdaloid kindled seizures in rats. Brain research 706**:** 173-176.

Talos DM, Follett PL, Folkerth RD, Fishman RE, Trachtenberg FL, Volpe JJ, *et al.* (2006). Developmental regulation of alpha-amino-3-hydroxy-5-methyl-4-isoxazole-propionic acid receptor subunit expression in forebrain and relationship to regional susceptibility to hypoxic/ischemic injury. II. Human cerebral white matter and cortex. The Journal of comparative neurology 497**:** 61-77.

Tateno M, Sadakata H, Tanaka M, Itohara S, Shin RM, Miura M, *et al.* (2004). Calcium-permeable AMPA receptors promote misfolding of mutant SOD1 protein and development of amyotrophic lateral sclerosis in a transgenic mouse model. Human molecular genetics 13**:** 2183-2196.

Traynelis SF, Wollmuth LP, McBain CJ, Menniti FS, Vance KM, Ogden KK, *et al.* (2010). Glutamate receptor ion channels: structure, regulation, and function. Pharmacol Rev 62**:** 405-496.

Twomey EC, & Sobolevsky AI (2018). Structural Mechanisms of Gating in Ionotropic Glutamate Receptors. Biochemistry 57**:** 267-276.

Twomey EC, Yelshanskaya MV, Grassucci RA, Frank J, & Sobolevsky AI (2017). Channel opening and gating mechanism in AMPA-subtype glutamate receptors. Nature 549**:** 60-65.

Twomey EC, Yelshanskaya MV, Vassilevski AA, & Sobolevsky AI (2018). Mechanisms of Channel Block in Calcium-Permeable AMPA Receptors. Neuron 99**:** 956-968 e954.

Van Damme P, Braeken D, Callewaert G, Robberecht W, & Van Den Bosch L (2005). GluR2 deficiency accelerates motor neuron degeneration in a mouse model of amyotrophic lateral sclerosis. Journal of neuropathology and experimental neurology 64**:** 605-612.

Venkataramani V, Tanev DI, Strahle C, Studier-Fischer A, Fankhauser L, Kessler T, *et al.* (2019). Glutamatergic synaptic input to glioma cells drives brain tumour progression. Nature 573**:** 532-538.

Venkatesh HS, Morishita W, Geraghty AC, Silverbush D, Gillespie SM, Arzt M, *et al.* (2019). Electrical and synaptic integration of glioma into neural circuits. Nature 573**:** 539-545.

Wang J, Wang W, Kollman PA, & Case DA (2001). Antechamber: an accessory software package for molecular mechanical calculations. J Am Chem Soc 222**:** U403.

Wang J, Wolf RM, Caldwell JW, Kollman PA, & Case DA (2004). Development and testing of a general amber force field. Journal of computational chemistry 25**:** 1157-1174.

Warren EC, Walker MC, & Williams RSB (2018). All You Need Is Fats-for Seizure Control: Using Amoeba to Advance Epilepsy Research. Front Cell Neurosci 12**:** 199.

Weiss JH (2011). Ca permeable AMPA channels in diseases of the nervous system. Frontiers in molecular neuroscience 4**:** 42.

Whitehead G, Regan P, Whitcomb DJ, & Cho K (2017). Ca(2+)-permeable AMPA receptor: A new perspective on amyloid-beta mediated pathophysiology of Alzheimer's disease. Neuropharmacology 112**:** 221-227.

Wilding TJ, Chai YH, & Huettner JE (1998). Inhibition of rat neuronal kainate receptors by cis-unsaturated fatty acids. J Physiol 513 (Pt 2)**:** 331-339.

Wilding TJ, Chen K, & Huettner JE (2010). Fatty acid modulation and polyamine block of GluK2 kainate receptors analyzed by scanning mutagenesis. J Gen Physiol 136**:** 339-352.

Wilding TJ, Fulling E, Zhou Y, & Huettner JE (2008). Amino acid substitutions in the pore helix of GluR6 control inhibition by membrane fatty acids. J Gen Physiol 132**:** 85-99.

Wlaz P, Socala K, Nieoczym D, Zarnowski T, Zarnowska I, Czuczwar SJ, *et al.* (2015). Acute anticonvulsant effects of capric acid in seizure tests in mice. Prog Neuropsychopharmacol Biol Psychiatry 57**:** 110-116.

Wollmuth LP, & Sobolevsky AI (2004). Structure and gating of the glutamate receptor ion channel. Trends Neurosci 27**:** 321-328.

Yelshanskaya MV, Li M, & Sobolevsky AI (2014). Structure of an agonist-bound ionotropic glutamate receptor. Science 345**:** 1070-1074.

Yelshanskaya MV, Singh AK, Sampson JM, Narangoda C, Kurnikova M, & Sobolevsky AI (2016). Structural Bases of Noncompetitive Inhibition of AMPA-Subtype Ionotropic Glutamate Receptors by Antiepileptic Drugs. Neuron 91**:** 1305-1315.

Yin HZ, Hsu CI, Yu S, Rao SD, Sorkin LS, & Weiss JH (2012). TNF-alpha triggers rapid membrane insertion of Ca(2+) permeable AMPA receptors into adult motor neurons and enhances their susceptibility to slow excitotoxic injury. Experimental neurology 238**:** 93-102.

Yuan CL, Shi EY, Srinivasan J, Ptak CP, Oswald RE, & Nowak LM (2019). Modulation of AMPA Receptor Gating by the Anticonvulsant Drug, Perampanel. ACS Med Chem Lett 10**:** 237-242.

Table 1. Data collection and refinement statistics.

	GluA2$_{Del}$-4BCCA
PDB accession code	6XSR
Data Collection	
Beamline	APS-24ID-C
Space group	$P2_12_12_1$
Cell dimensions	
a, b, c, (Å)	92.8, 110.4, 600.1
α, β, γ (^{0})	90, 90, 90
Wavelength (Å)	0.92
Resolution (Å)	48.91-4.25
Completeness (%)*	99.53 (99.77)
Redundancy*	9.82 (7.53)
|I/σ|*	9.35 (1.45)
R_{meas} (%)*	8.34 (103)
$CC_{1/2}$*	99.7 (65.7)
Refinement	
Resolution (Å)	4.25
Completeness (%)*	99.53 (99.77)
Number of reflections*	44507 (4352)
R_{work}/R_{free}*	0.2560 (0.3629)/ 0.2924 (0.3633)
Number of atoms	
Total	3799
Ligand	82
B-factor (Å^2)	
Protein	257.5
Ligand	269.7
RMS deviations	
Bond length (Å)	0.003
Bond angles (^{0})	0.50
Ramachandran	
Favored (%)	92.0
Allowed (%)	7.3
Disallowed (%)	0.7

*Highest resolution shell in parentheses.

5% of reflections were used for calculation of R_{free}.

Table 2. 4-BCCA interactions with key residues.

Protein	Ligand	Contact Frequency (%)										
		F584	Residue 585	Residue 610 adjacent subunit	Residue 610 adjacent subunit	I611 adjacent subunit	I613	I613 adjacent subunit	I613 adjacent subunit	I613 opposite subunit	Residue 614 adjacent subunit	Residue 614 adjacent subunit
WT	A	-	-	97.60	-	67.20	73.80	-	-	-	97.80	-
	B	64.00	-	82.40	-	79.60	87.40	-	-	-	-	-
	C	-	-	54.80	-	76.20	-	-	-	-	60.60	-
	D	77.20	57.60	56.20	-	90.00	86.20	50.60	-	-	99.60	-
L610F	A	92.40	89.60	97.00	-	-	79.80	-	-	-	-	-
	B	-	-	100.00	-	84.40	99.00	-	-	-	97.80	-
	C	59.60	-	67.20	-	85.60	88.80	-	-	-	-	-
	D	51.40	-	-	-	-	-	-	-	-	-	-
S614L	A	-	-	80.22	-	95.60	53.63	-	-	-	-	-
	B	61.32	-	70.11	-	76.48	-	-	-	-	60.22	-
	C	94.07	86.15	-	-	-	-	-	-	-	-	-
	D	66.59	79.12	100.00	-	-	79.34	59.56	-	-	85.05	-
S614Q	A	86.17	-	87.07	-	66.21	75.28	-	-	-	82.54	-
	B	-	-	74.60	-	-	64.40	-	-	-	86.39	74.38
	C	-	54.88	90.48	-	74.60	76.19	-	-	-	99.77	-
	D	57.60	-	71.43	-	82.77	75.06	-	-	-	78.68	-
S614N	A	92.40	-	73.80	-	81.60	87.60	-	-	-	-	-
	B	-	-	72.00	-	97.20	77.40	-	-	-	96.60	-
	C	-	-	79.40	59.00	-	85.20	-	65.00	80.20	86.00	97.60
	D	-	-	80.00	-	87.20	79.80	-	-	-	74.20	-
M585W	A	89.00	-	82.20	-	84.80	95.60	-	-	-	-	-
	B	-	-	81.40	-	90.00	87.80	-	-	-	77.60	-
	C	54.20	-	64.40	-	67.20	70.60	-	-	-	95.40	-
	D	-	-	-	93.20	-	-	-	89.60	74.40	-	65.00
M585A	A	65.60	-	97.80	-	84.60	86.40	-	-	-	70.80	-
	B	-	-	82.60	-	92.00	92.80	-	-	-	74.20	-
	C	65.80	-	78.60	-	84.00	73.80	-	-	-	75.20	-
	D	97.20	-	77.40	-	88.60	88.60	-	-	-	-	-

Contact frequencies between 4-BCCA and key protein residues in all mutant simulations and an example wild type simulation. Contacts that lasted for less than 50% of the simulation are not shown. Ligands that entered the channel pore are marked with asterisks (*).

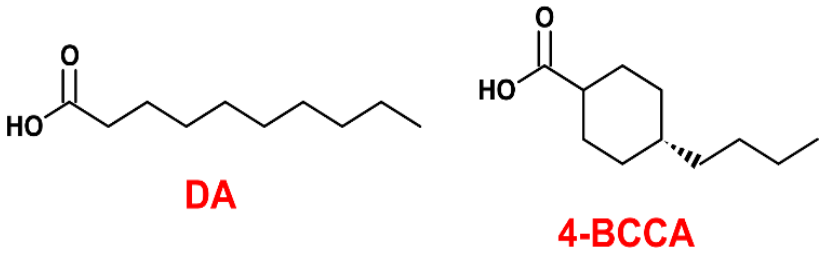

Figure 1. Chemical structures of decanoic acid (DA) and trans-4-butylcyclohexane carboxylic acid (4-BCCA).

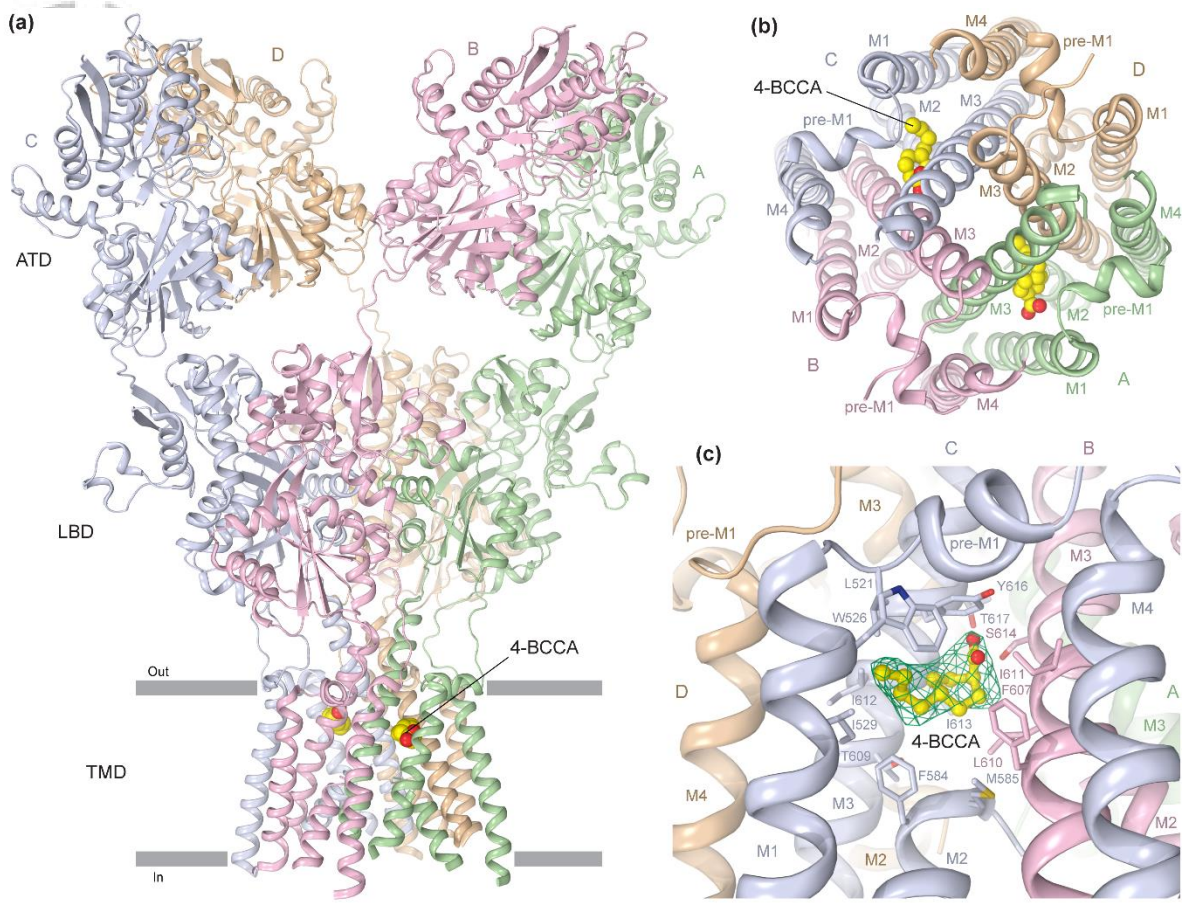

Figure 2. Structure of AMPA receptor in complex with 4-BCCA. (**a**) $GluA2_{4\text{-BCCA}}$ structure viewed parallel to the membrane and perpendicular to the overall two-fold axis of molecular symmetry. Each subunit is in different colour. Inner and outer sides of membrane are indicated by parallel grey bars. 4-BCCA molecules are shown in space-filling representation. (**b**) Transmembrane domain viewed extracellularly, along the overall two-fold axis of molecular symmetry. (**c**) Close-up view of 4-BCCA binding site in the side portal between subunits C and B. 4-BCCA molecule is shown in ball-and-stick representation. Green mesh shows positive electron density for 4-BCCA in the Fo-Fc omit map contoured at 3σ.

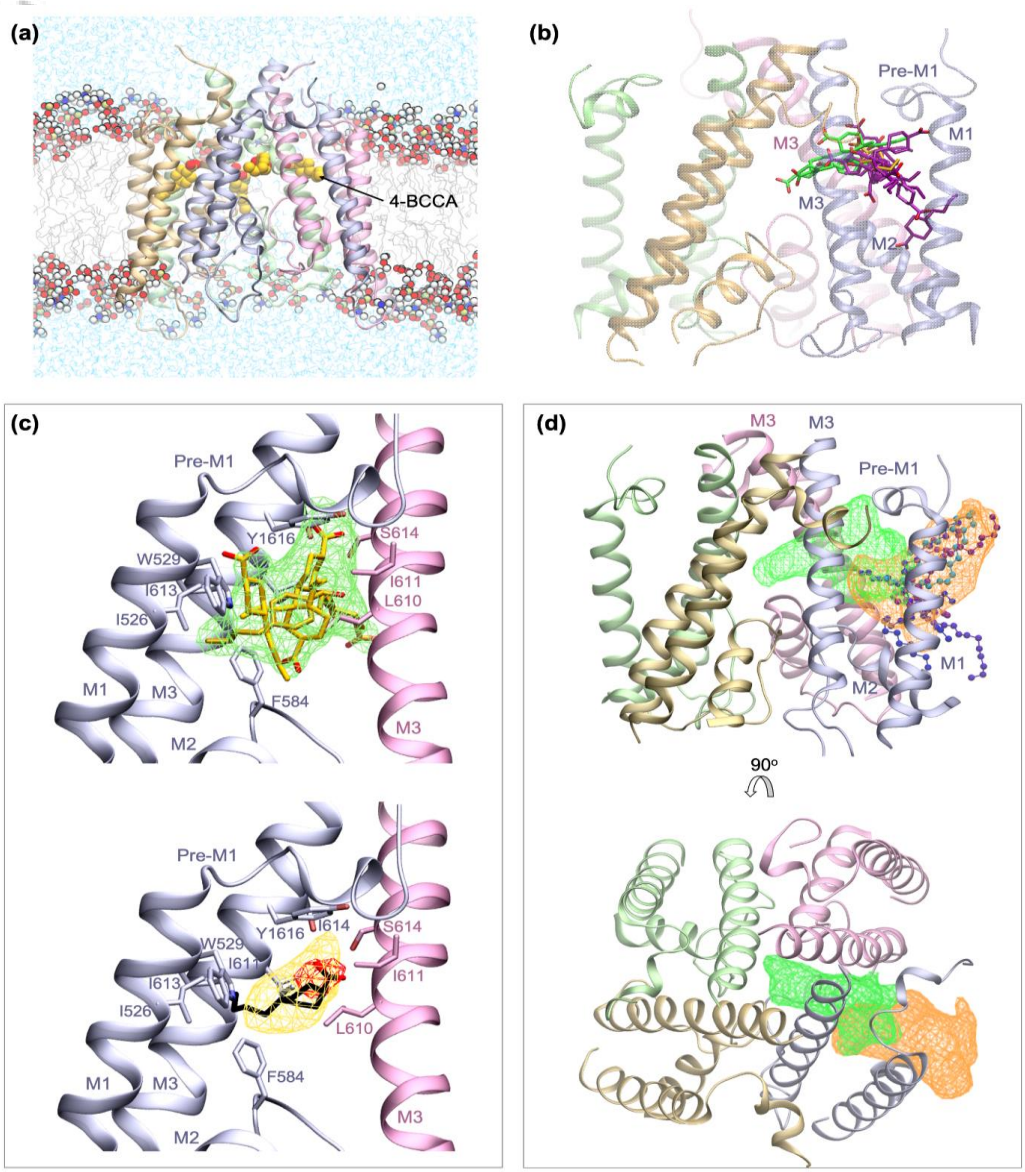

Figure 3. MD simulations of AMPA receptor in complex with 4-BCCA. (**a**) Simulated $GluA2_{4\text{-}BCCA}$ system in POPC lipid membrane and water. Protein subunits are shown in different colours. 4-BCCA molecules are shown in space-filling representation. Some lipids and waters are removed for clarity. (**b**) Representative positions of protonated (purple) and deprotonated (green) 4-BCCA from all simulations overlapped with the two crystal structure poses (yellow). Deprotonated ligands that did not remain in the binding region are not shown. (**c**) Top: density for 4-BCCA averaged over all simulations (green mesh) with several representative ligand orientations (yellow sticks). Bottom: the region with the highest ligand density in simulations representing the most likely orientation of 4-BCCA (mesh) overlapped with crystal pose (black sticks). Red and yellow regions of density represent polar/charged and hydrophobic regions of 4-BCCA, respectively. (**d**) Average lipid density at the binding site from four GluA2 simulations in the absence 4-BCCA (orange mesh) overlapped with ligand density from all $GluA2_{4\text{-}BCCA}$ simulations (green mesh). Density plots were created using VolMap tool of VMD with an isovalue of 0.05 based on the positions of ligand/lipid heavy atoms. The lipid molecules shown in colored ball and stick representation are taken from a single simulation for illustrative purposes.

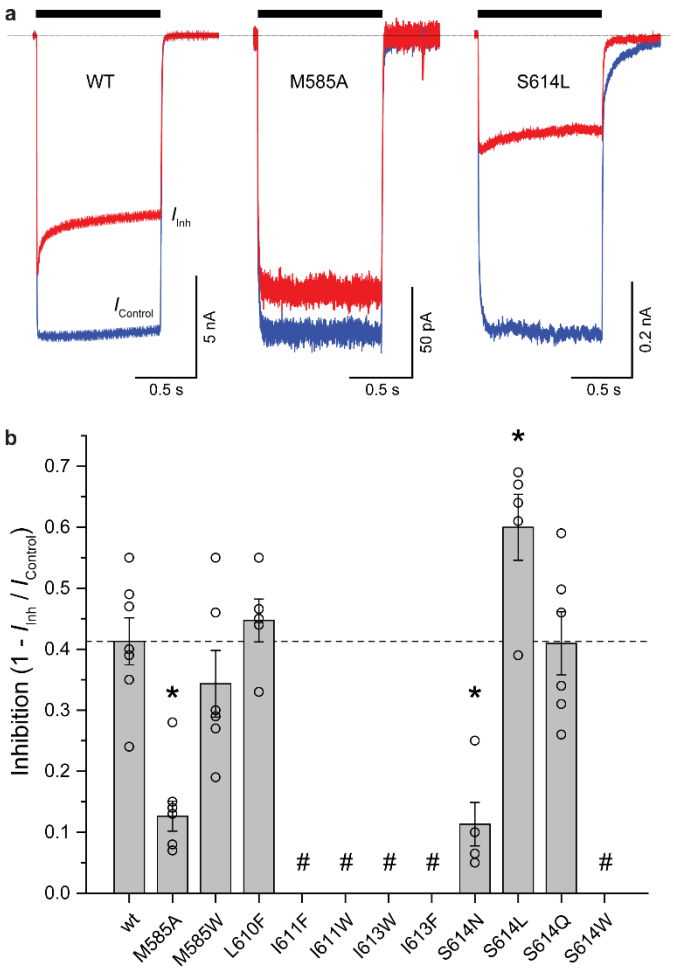

Figure 4. Mutagenesis at the 4-BCCA binding site. (**a**) Examples of whole-cell currents recorded in the continuous presence of 30 µM cyclothiazide at –60 mV membrane potential from HEK293 cells expressing $GluA2_{WT}$, $GluA2_{M585A}$ or $GluA2_{S614L}$ in response to 1 s applications (black bars) of 3 mM Glu alone (blue) or co-applications of 3 mM Glu and 2 mM 4-BCCA (red). (**b**) Extent of current inhibition by 4-BCCA measured for wild type and mutant GluA2 (mean ± SEM), with individual measurements shown as the open circles. Symbols # indicate that the corresponding mutants did not show measurable currents and * statistically different extent of inhibition for the mutant compared to wild type GluA2 (t-Test, $P < 0.05$, n = 5-8).

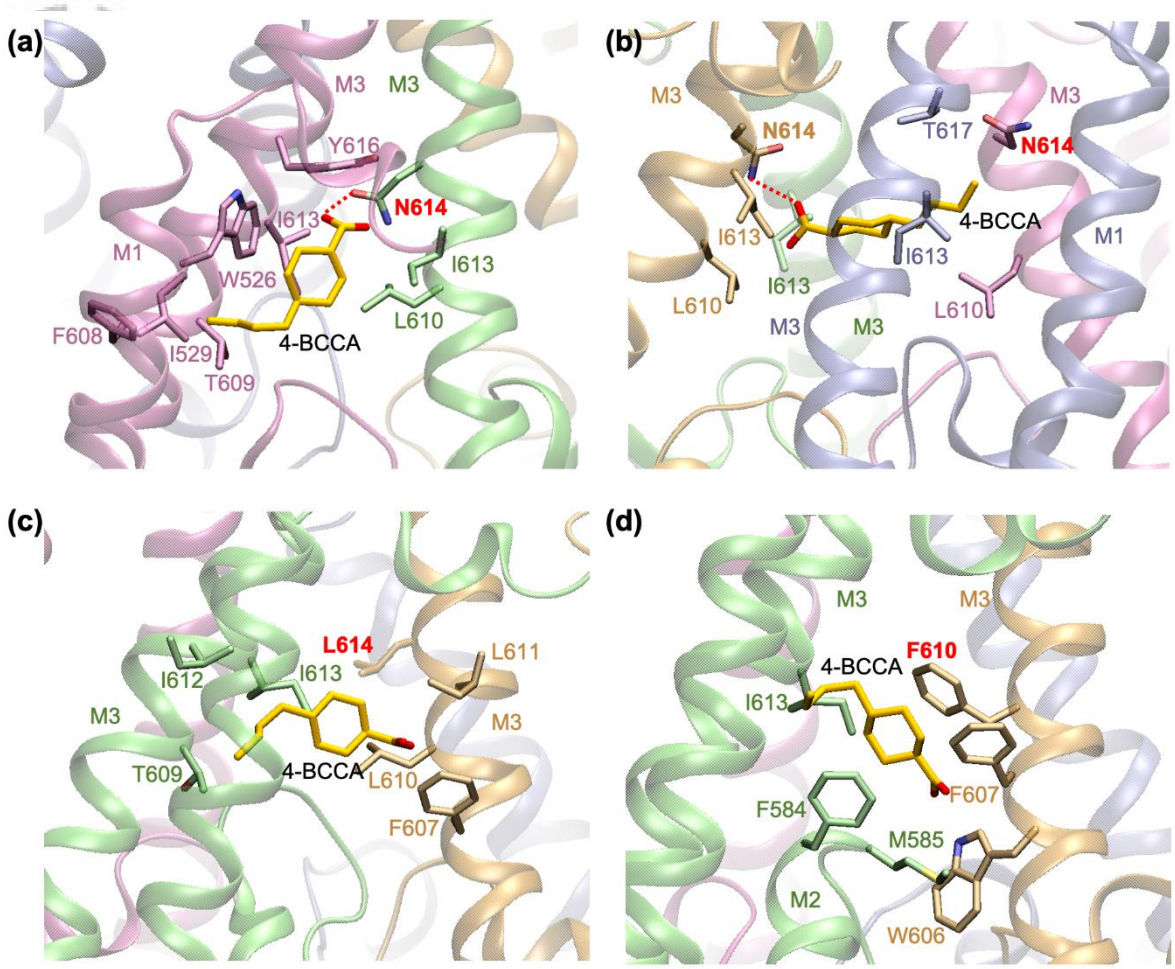

Figure 5. MD simulations of AMPA receptor mutants in complex with 4-BCCA. The panels illustrate 4-BCCA modes of binding to GluA2 mutants, with mutated residues (red labels) and residues that interact with 4-BCCA shown. Hydrogen bonds between 4-BCCA and protein residues are shown as red dashed lines. (**a**) 4-BCCA at the binding site in S614N mutant. (**b**) 4-BCCA that entered the channel pore in S614N mutant. (**c**) 4-BCCA at the binding site in S614L mutant. Note that 4-BCCA does not interact with the mutated residue. (**d**) 4-BCCA at the binding site in L610F mutant.

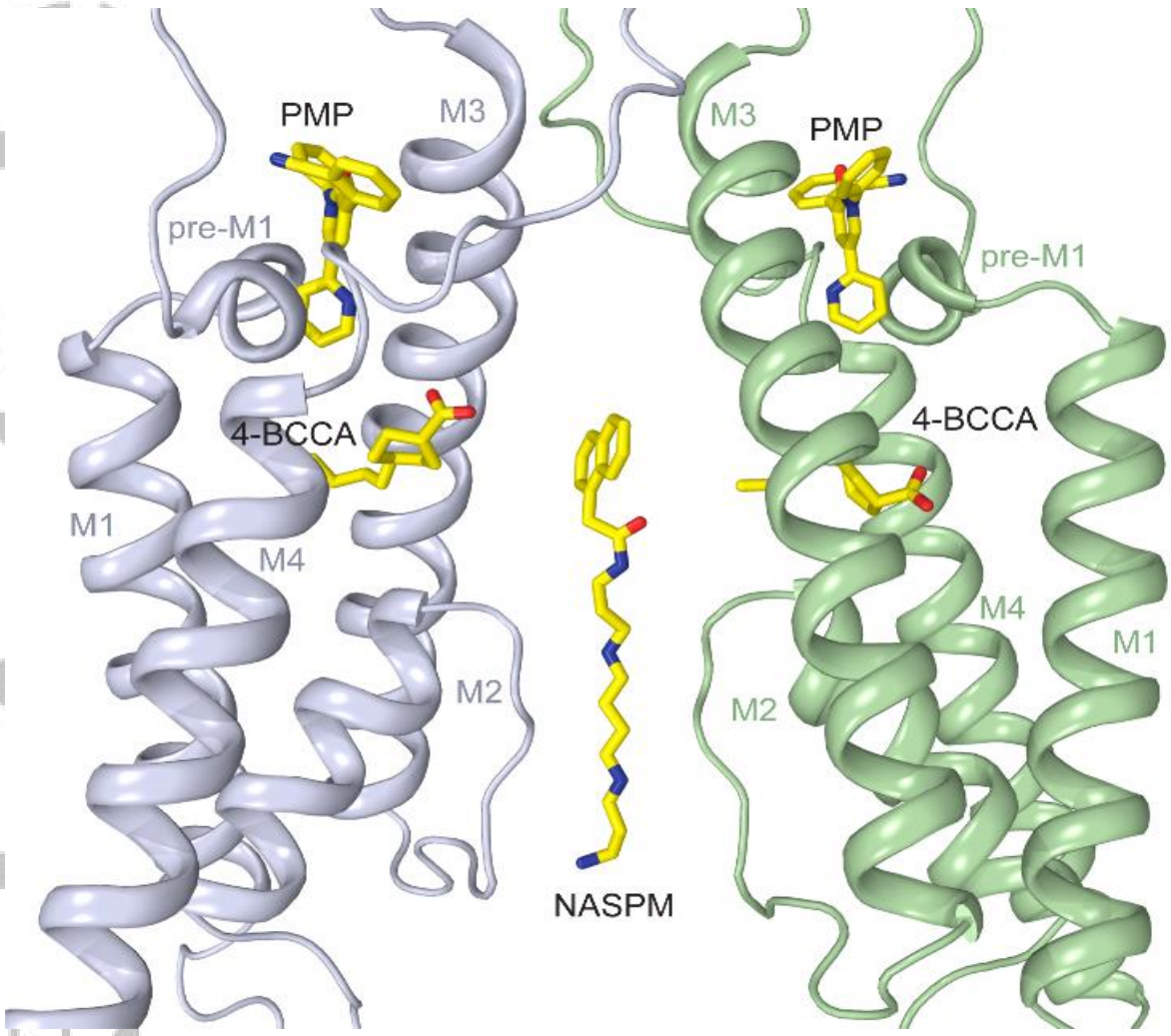

Figure 6. Binding sites of 4-BCCA, PMP and NASPM in the TMD of AMPA receptor. The TMD is viewed parallel to the membrane, with the front and back subunits (B and D) removed for clarity. Molecules of 4-BCCA, PMP and NASPM are in stick representation (yellow).